Received: 12 January 2025 | Revised: 14 May 2025 | Accepted: 8 June 2025

DOI: 10.1111/jace.70046

Journal of the American Ceramic Society

RESEARCH ARTICLE

One-pot instant flame synthesis of strontium-doped lanthanum nickelate perovskite for energy conversion and storage

Laxman Singh[1] | **Vineet Kumar Patel**[1] | **Ayan Mukherjee**[2] | **Varsha Singh**[3] | **Anup Kumar**[4] | **Abhishek Rai**[5] | **Vellaichamy Ganesan**[3] | **Anshuman Srivastava**[6] | **Parwathi Pillai**[7] | **Rajeev Kumar**[8] | **R. N. Rai**[3] | **Youngil Lee**[9]

[1]Department of Chemistry, Siddhartha University, Kapilvastu, Siddharth Nagar, Uttar Pradesh, India

[2]Department of Physics, College of Commerce, Arts & Science, Patliputra University, Patna-20, India, Patna, Bihar, India

[3]Department of Chemistry, Institute of Science, Banaras Hindu University, Varanasi, Uttar Pradesh, India

[4]Department of Chemistry, Indian Institute of Technology (Banaras Hindu University), Varanasi, Uttar Pradesh, India

[5]Department of Chemistry, L.N. Mithila University Darbhanga, Darbhanga, Bihar, India

[6]Indian Institute of Packaging Lucknow, Govt. of India, Lucknow, Uttar Pradesh, India

[7]Department of Chemical Engineering, Swarrnim Startup & Innovation University, Gandhinagar, Gujarat, India

[8]Department of Chemistry and Biochemistry, North Carolina Central University, Durham, North Carolina, USA

[9]Chemical Industry Research Institute, Core Research Institute, University of Ulsan, Ulsan, Republic of Korea

Correspondence
Youngil Lee, Chemical Industry Research Institute, Core Research Institute, University of Ulsan, Ulsan 44776, Republic of Korea.
Email: nmryil@ulsan.ac.kr

Abhishek Kumar Rai, Department of Chemistry, L.N. Mithila University Darbhanga 846008, Bihar, India.
Email: abhishekraiinorg@gmail.com

Laxman Singh, Department of Chemistry, Siddhartha University, Kapilvastu, Siddharth Nagar 272202, Uttar Pradesh, India.
Email: laxmanresearcher@suksn.edu.in

Funding information
National Research Foundation of Korea (MSIT), Grant/Award Number: 2021R1A2C1010373; MOE, Grant/Award Number: 2021R1A6A1A03038858; Siddharth University for the minor project, Grant/Award Number: SMGFOC/2023-24/FS-005; Council of Science and Technology, Lucknow, Uttar Pradesh, Grant/Award Number: 4287

Abstract

Perovskite structures have great potential to act as multifunctional electrocatalysts with excellent surface chemistry, reactivity, and electrode kinetics for energy storage and conversion. It is a big challenge to fabricate the bulk perovskite material using low-cost and eco-friendly synthetic route along with desirable characteristics, that is, exposed active sites. To address this issue, we synthesized an important model perovskite material, viz. $La_{1.85}Sr_{0.15}NiO_4$ (LSNO), using an instantaneous flame synthesis technique. The current synthesis procedure is a rapid and economical technique regarding raw material cost, synthesis duration, and energy consumption, thereby eliminating the usual multi-step processing compared to other reported techniques so far. The synthesized LSNO has been characterized using various physico-chemical techniques such as thermogravimetric analyses (DTA/TG), X-ray diffraction (XRD), Fourier transform infrared (FT-IR), Raman spectroscopy, X-ray photoelectron spectroscopy (XPS), electron microscopy (SEM/TEM), etc. XRD analysis confirmed the formation of a single phase of LSNO after sintering at 900°C for 12 h. In FT-IR spectra, the absorption bands were noticed at 520, 664, and 880 cm^{-1} corresponding to the La–O, Ni–O, and Sr–O vibrations. The energy dispersive X-ray spectroscopy (EDX) and XPS studies showed the presence of La, Sr, Ni, and O elements which confirm the purity and stoichiometry of LSNO. Here, we report the quick and hassle-free syn-

thesis. LSNO showed excellent oxygen reduction reaction (ORR) activity with an onset potential of 0.88 V versus Reversible Hydrogen Electrode (RHE), which is lower than several existing perovskite-based electrocatalysts. This sample could also be used as supercapacitor material. The galvanostatic charge/discharge test showed stability even at high current densities with a capacity retention of 97.25% even after 500 cycles. The superior ORR activity and electrochemical performance of LSNO provides an impetus for exploring this economical approach toward perovskite-based material synthesis for energy conversion and storage applications.

KEYWORDS
electrochemical energy storage, flame synthesis, fuel cell, oxygen reduction reaction, perovskite, supercapacitor

1 | INTRODUCTION and BACKGROUND

The modern era of advanced energy storage and conversion systems has great potential toward the growing market for smart electronics and electrical vehicles (EVs).[1] The continuous global industrial growth needs the mass production and evolution of environment-friendly, economical, portable, and green/renewable energy conversion and storage systems with high power and energy densities.[2,3] There are numerous energy storage and conversion systems such as batteries (Li-ion, Na-ion, lead acid, metal air, etc.), supercapacitors (SCs), solar cells, fuel cells (FCs), and capacitors.[4] To meet the demand of environment-friendly, high-energy density, high power density, and excellent stability, FCs and SCs are the two most promising energy storage candidates for electronics devices and EVs.

Design of suitable electrode materials for robust electrocatalysis is still challenging in energy storage and conversion systems.[5] Several types of electrode materials are being investigated, including carbon based (graphene, nanotubes, etc.), transition metal dichalcogenides, MXene, oxide, layered perovskites, etc. Cationic substitution is a great tool to enhance electrocatalytic reactions in oxide/perovskite materials.[6] Moreover, the tunable bandgap, excellent conductivity, feasible mechanical characteristics, hydrophilicity, abundant active sites and tunable electrochemical features make MXene structure suitable, but aggregation and restacking of its layers prove a hindrance. This leads to the prospective development of other promising and functional materials for FCs and SC applications.[7] Moreover, multifunctional composite materials are better alternatives for simultaneously providing structural stability and improved electrochemical properties.[8]

The cathode is the main intrinsic component of FCs and SCs energy storage devices on which the power density, energy density, and efficiency of the system depend. Nowadays, a trend has emerged to utilize the multifunctional materials as the potential candidates for the various device components to perform robust functions in a plethora of industrial applications, that includes energy, medicine, nanoelectronics, aerospace, defence, semiconductor, among others.[9,10] The multifunctionality of these materials mainly relies on the properties such as electrical, magnetic, electrochemical, optical, mechanical, etc.[11] These multifunctional materials have tremendous potential to impact new system performance in any field (especially in energy storage and conversion) by reducing size, cost, and complexity while improving catalytic efficiency, safety, and versatility.[12]

In the case of energy conversion, FCs have received much research attention, but constant efforts are needed to effectively apply them in industry. The main disadvantage of FCs is the need for high operating temperatures,[13] which leads to accelerated performance degradation and imposes strong demands on the materials that impede long-term stability.[14] Till date, platinum/carbon (Pt/C) and other Pt-based materials have been considered as state-of-the-art catalysts for the oxygen reduction reaction (ORR).[15] However, the use of FCs is limited by the slow ORR activity at the cathode[16] and the high cost of noble metal-based catalysts used. On the other hand, non-noble metal-based catalysts, especially transition metals as Mn, Co, Fe, and Ni, are attracting significant interest due to their high abundance and low cost, but the slow kinetics in ORR and oxygen evolution reaction (OER) still pose a challenge to commercialize the FCs.

On the other hand, SCs play a vital role in futuristic electrochemical energy storage devices which require

high power density. The energy density, specific capacity, capacity retention, and thermal stability mainly depend on the electrode material. The scientists and technologists have started to explore the various perovskites mixed with noble metals because it offers low cost, good electrical conductivity, and transport electrons that result from oxidation/reduction to the current collectors. Although perovskites are abundant and cost-effective, their electrical conductivity is low. To overcome these disadvantages, various composite materials are being investigated for FCs and SCs. By combining perovskite oxides with noble metals, it is expected to improve the performance of SCs through synergistic effects.[17] Among them, perovskite materials based on the ABO_3 formula (where A and B are cations of different sizes and O is the anion)[18] may be potential candidates as electrode materials for FCs as well as SCs. Therefore, there is a need to develop advanced materials that can show good performance for both SC electrodes and electrochemical water splitting systems simultaneously. The materials should also be low-cost and easy to synthesize for the mass production for commercial applications.

Herein, we investigate the $La_{1.85}Sr_{0.15}NiO_4$ (LSNO) perovskite material as a multifunctional cathode material for FCs as well as electrode material for SCs. The perovskite structure of LSNO is very helpful in designing high energy-density based SC electrodes.[19] As per reported earlier literature, Sr-doped $LaNiO_3$ via the sol–gel method maintains significant porosity in this perovskite structure by precisely utilizing the Sr dopants. The doping increases specific capacitance as well as retentivity.[20] Perovskite oxides show the pseudo-capacitance behavior and the oxygen vacancies of the material should be the charge storage sites. Thus, the number of oxygen vacancies can be increased to maximize the energy density. In bulk material, the oxygen vacancies can be changed by partially substituting supplementary metal ions in the B-sites. In the current studies, the Sr^{2+} doping distinctly increased its oxygen vacancies.[21] In addition, perovskites have been shown to have better photovoltaic and energy storage capabilities than various other transition metal compounds and even some precious metal oxides. However, further improvement in perovskite performance is required, facilitated by the preparation methods, substitutions, enhancement of electronic conductivity, assembly process, and selection of proper electrolytes.[22] Lanthanum nickelates ($LaNiO_3$) belong to a relatively new family of nickelate-based compounds. Additionally, there are multiple derivatives of this structure including Ruddlesden–Popper (RP) oxides that have a crystal structure represented as $A_{n+1}B_nO_{3n+1}$ or equivalently $(AO)(ABO_{3+\delta})_n$, where $n(BO_6)$ octahedra perovskite layers are separated by rock salt (AO)(OA) double layers. Oxygen diffusion through vacancies within the perovskite lattice or through the rock salt layer of the RP structure aided in the exceptional performance of these oxides toward the OER.[23,24] These materials exhibit various electrochemical, magnetic, electrical, optical, and electronic properties, making it a promising candidate as electrode material for FCs and SCs. The present research article for the first time emphasizes the multi-faceted nature of lanthanum nickelates, RP oxides by providing ease of fabrication, structural stability, highly crystalline structures, and a discussion of its significance in energy conversion systems for FCs and electrochemical energy storage for SCs. So far, only a few works on dielectric and ferroelectric properties of lanthanum nickelates have been reported. However, a study by Cao et al.[19] reported the formation process of lanthanum nickelates and Sr-doped lanthanum nickelates through direct oxidation, but it degraded the electrochemical abilities. As such, special attention is placed on the strategic synthesis method of lanthanum nickelates and its energy applications for modern devices such as FCs and SCs. In addition, easy fabrication of doped lanthanum nickelates is sought after.

We report the flame synthesis technique to fabricate the LSNO for the first time. Although there are several traditional techniques reported so far for the synthesis of lanthanum nickelates, for example, traditional solid-state route, soft-chemical routes such as co-precipitation, sol–gel, and hydrothermal etc., but the above-mentioned techniques require tedious work, cumbersome handling, multistep, complex methodologies and utilizing high energy and long-time during synthesis process. The current synthesis process takes only a few minutes from weighing the metal nitrates precursor to obtaining the precursor powder of LSNO (~55–65 min), unlike the traditional solid-state route (~10–60 h) and wet chemical methods (~10–55 h).

2 | EXPERIMENTAL

2.1 | Material synthesis

$La_{1.85}Sr_{0.15}NiO_4$ (LSNO) was synthesized using a temperature-induced rapid automatic flame synthesis method. The process is efficient, simple, and saves time and energy, making it promising for large-scale production of LSNO. The chemicals used in the synthesis $La(NO_3)_3.6H_2O$ (Alfa Aesar, 99.90%), $Sr(NO_3)_2$ (Alfa Aesar, 98.00%), $Ni(NO_3)_2.6H_2O$ (Sigma Aldrich, 98.50%), and 2-methoxyethanol (Alfa Aesar, 99.50%) were of analytical grade and used without further purification. The stoichiometric amounts of La^{3+} (13.5451 g), Sr^{2+}(0.4498 g), and Ni^{2+} (4.9187 g) metal nitrates were dissolved in a ~150 mL amount of 2-methoxyethanol in a beaker, sonicated for 10–15 min, and heated on a hot plate with a

magnetic stirrer at 120°C–150°C to vaporize the organic solvent. The ignition of metal ions resulted in the release of a huge quantity of gas and a greenish flame. Within 15–20 s, a fluffy precursor powder of $La_{1.85}$ $Sr_{0.15}NiO_4$ (LSNO) was produced. Videos of the flame synthesis process can be found in the supplementary information (Supplementary Video SV1). The obtained product was ground using a pestle and mortar and sintered at 900°C for 12 h in an ordinary electric furnace without pre-calcination.

2.2 | Materials characterization

The crystalline structure of the $La_{1.85}$ $Sr_{0.15}NiO_4$ sintered powder, which was heated at 900°C for 12 h, was analyzed using X-ray diffraction (XRD, Rigaku Ultima IV, Japan) with Cu K_α radiation. Rietveld refinement of XRD data using FULL-PROOF Software with a peak shape of pseudo-Voigt in the 2θ (°) region of 20°–80° was done to examine the phase identification of LSNO. The morphology and composition were examined using a scanning electron microscope (SEM, JEOL JSM6500F, Japan) equipped with energy-dispersive X-ray spectroscopy (EDX) for elemental analysis. X-ray photoelectron spectroscopy (XPS, Thermo Fisher Kα, USA) was conducted to investigate the constituents and oxidation states of the material. Fourier transform infrared (FT-IR, Shimadzu IRAffinity-1S, Japan) spectra were obtained using KBr pellets with an appropriate component range from 400 to 1600 cm^{-1}. Raman spectra with a resolution of 4 cm^{-1} were collected using a Raman microscope with a diode laser (λ_{ex} = 785 nm, power = 44 mW), a CCD detector, and a holographic grating (Kaiser Optical Inc., USA). The samples were placed on a microscope stage, and the laser beam was focused using a 10×/0.25NA objective lens to collect the spectra. The particle size and crystallinity of the material were analyzed using a transmission electron microscope (TEM, JEM-2100F, Japan). The Brunauer–Emmett–Teller (BET) surface area analysis of the LSNO was performed to determine the pore size distribution. Analysis was done by using XRD, FE-SEM, and EDX at the total-period analysis center for Ulsan Chemical Industry of Korea Basic Science Institute (KBSI).

2.3 | Electrochemical characterization

2.3.1 | Fuel cell

The glassy carbon electrode (GCE) with an area of 0.196 cm^2 was cleaned by using 0.05-μm alumina powder and sonicated for 30 s, then left to air dry. The electrode was then coated with a 1.0% suspension of $La_{1.85}Sr_{0.15}NiO_4$, which was fabricated by dispersing 10 mg of LSNO material in 1.0 mL of *N*, *N*-dimethylformamide (DMF). The suspension was sonicated for 30 min before being applied to the GCE, resulting in the creation of a GCE/LSNO modified electrode.

2.3.2 | Supercapacitor

Electrochemical measurements were conducted using a two-electrode system in a 1 M Na_2SO_4 electrolyte solution. The sample was prepared by mixing active material, acetylene black, and polytetrafluoroethylene in the ratio of 80:10:10 and dispersing the mixture into isopropanol. The solution was then dropped onto two 1 mm thick glass microfiber filter plates. A separate uncoated glass microfiber filter served as a separator between the two electrodes, and 1 M Na_2SO_4 was used as the electrolyte. The experiments were performed at a constant current density of 1 A g^{-1} with various scan rates, and the charge–discharge experiment was carried out at a 1 V DC bias voltage.

3 | RESULTS AND DISCUSSION

3.1 | Material characterization

The XRD patterns of LSNO shown in Figure 1 were analyzed to identify the crystallographic phase of the sample. The various peaks present at different particular 2θ angles were taken with the $LaNiO_3$ reference pattern (JCPDS 11-0557). The XRD pattern of LSNO at 2θ peaks: 24.2°, 28.4°, 31.5°, 33.4°, 42.8°, 44.6°, 46.7°, 53.03°, 56.1°, 58.5°, 65.5°, 68.9°, 76.02°, 77.5°, 85.6°, 88.5°, and 96.4° were respectively corresponding to (111), (004), (113), (020), (006), (024), (220), (131), (026), (227), (315), (028), (331), (111), (045), (242), and (139) Bragg peaks. The sharp peaks of the sample indicate its crystalline nature. The average crystallite size of the LSNO sample was determined using the Debye–Scherrer's equation ($d = 0.9\lambda/\beta \cos\theta$, where k is the Debye–Scherrer constant identical to 0.9, λ is the X-ray wavelength of 1.5406 Å, β is the full width at half maximum of the highest peak, and θ is the Bragg angle in radians) and was found to be 28 nm. Thus, the XRD results confirm that the LSNO sample was fabricated in this process.[16]

Moreover, Rietveld refinement of XRD data using FULL-PROOF Software with a peak shape of pseudo-Voigt in the 2θ (°) region of 20–80 was done to examine the phase identification of LSNO. The results are displayed in Figure 1B. As can be seen from the figure, there is an excellent match between the computed pattern (represented by the red circle) and the observed pattern (represented by the black

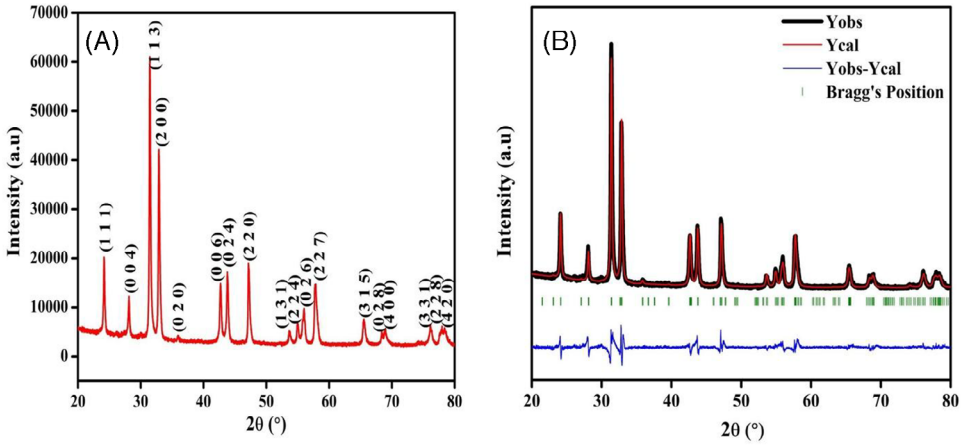

FIGURE 1 (A) Indicates XRD pattern and (B) represents Rietveld refinement of XRD data of LSNO perovskite. XRD, X-ray diffraction.

line), which perfectly overlaps. A positive confirmation of the single-phase development with tetragonal phase belonging to the space group *P42/ncm* (lattice parameter, $a = b = 5.450174$ Å and $c = 12.693995$ Å) was obtained by indexing all the peaks matching to LSNO with JCPDS card No. 11-0557 and also, further no additional peaks were observed during refinement of XRD data other than those of the host materials. The goodness of fit of XRD data for LSNO is also verified with the help of the lower value of goodness of fit (χ).[25] The following formulae were used to obtain the *R*-factors, which show the quality parameters of the fits and show good agreement between refined and experimental XRD data.[26]

$$R_p = \left(\frac{\sum_i | Y_{iobs} - Y_{ical}|}{\sum_i |Y_{iobs}|} \right) \times 100 \quad (1)$$

$$R_{wp} = \left(\frac{\sum_i W_{i.}(Y_{iobs} - Y_{ical})^2}{\sum_i W_{i.}(Y_{iobs})^2} \right)^{\frac{1}{2}} \times 100 \quad (2)$$

$$R_{exp} = \left(\frac{N - P}{\sum_i W_{i.}(Y_{iobs})^2} \right)^{\frac{1}{2}} \times 100 \quad (3)$$

$$\chi = \frac{R_{wp}}{R_{exp}}. \quad (4)$$

In this case, the profile factor, predicted profile factor, weighted profile factor, and goodness of fit of the XRD data are denoted by R_p, R_{exp}, R_{wp}, and χ, respectively. Additionally, the diffractogram's measured points, refined parameters, degrees of freedom, variance inverse, intensity computed at point 'i,' and intensity seen at point 'i' are denoted by the variables *N*, *P*, (*N*−*P*), W_i, Y_{iobs}, and Y_{ical}, respectively. All the refined parameters such as space group, lattice parameter (*a*,*b*,*c*), χ^2, *R*-factors in % (R_p, R_{exp}, R_{wp}), RF-factor (R_F), and Bragg's *R*-factors (R_{Bragg}) are disclosed in Table 1.

TABLE 1 Depicts refined parameters and reliability factor (R_p, R_{wp}, R_{exp}) of LSNO ceramic.

Formula	$La_{1.85}Sr_{0.15}NiO_4$
Cycles of refinement	20
2θ range (°)	20–80
Step (°)	0.010
χ^2	7.5
Crystal system	Tetragonal
Space group	*P42/ncm*
Crystallize size (nm)	128
Lattice parameters (*a*, *b*, *c*)	$a = b = 5.450174$ Å, and $c = 12.693995$ Å
V_{cell} (Å^3)	377.0674
FWHM (*U*,*V*,W) parameters	0.436574, −0.172672, 0.049379
R_p, R_{wp}, R_{exp} (%)	21.5, 19.6, 3.32
R_F, R_{Bragg} (%)	6.192, 4.921

The FT-IR transmittance spectra of the LSNO sample were recorded using ATR and are shown in Figure 2, which represents the chemistry and formation of the sample. As seen from the figure, the peaks of La–O, Ni–O, and Sr–O were respectively found at 520, 664, and 880 cm^{-1} due to symmetric vibrations. A strong COO bond at 2338 cm^{-1} reveals the formation of carboxylate, which increases the electrochemical activity. Furthermore, the peaks at 3735, 1750, and 1351 cm^{-1} correspond to CO_3^{2-}, COO^-, and C–O bonds. A peak representing OH bending of water was seen at 1630 cm^{-1} in the spectra. The FT-IR analysis implies that the LSNO sample has a lot of carboxyl groups, which would help increase the Faradaic reactions and eventually the supercapacitance.[27]

The SEM micrograph (Figure 3A) shows the morphology of LSNO. It exhibits an RP structure, consisting of perovskite Sr doped $LaNiO_3$ and LaO layers with

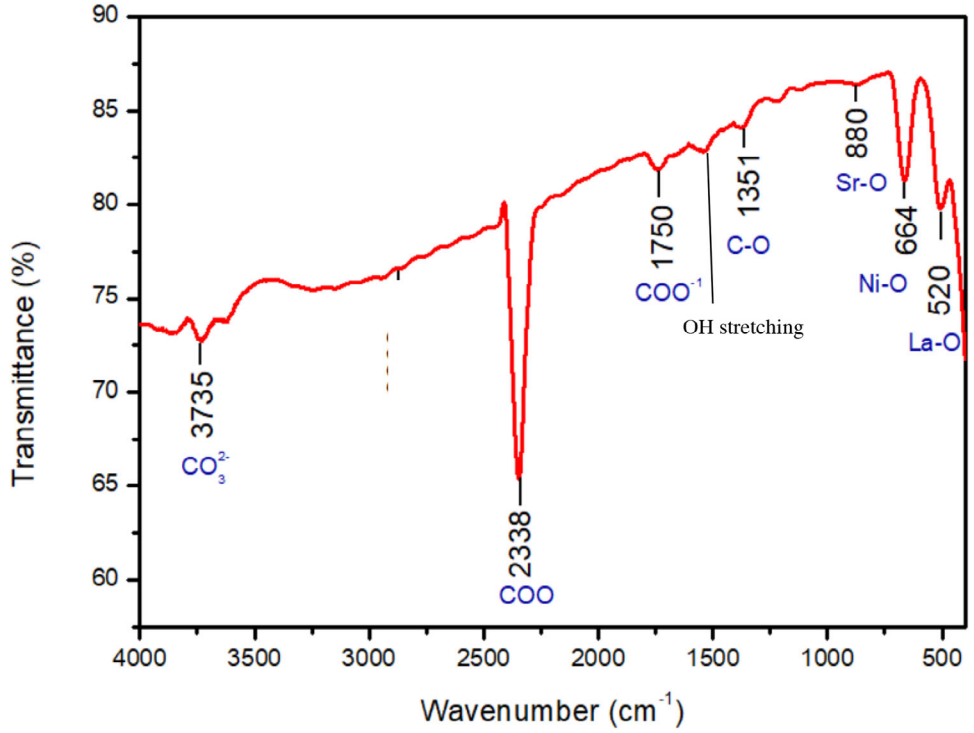

FIGURE 2 FT-IR spectrum of LSNO perovskite. FT-IR, Fourier transform infrared.

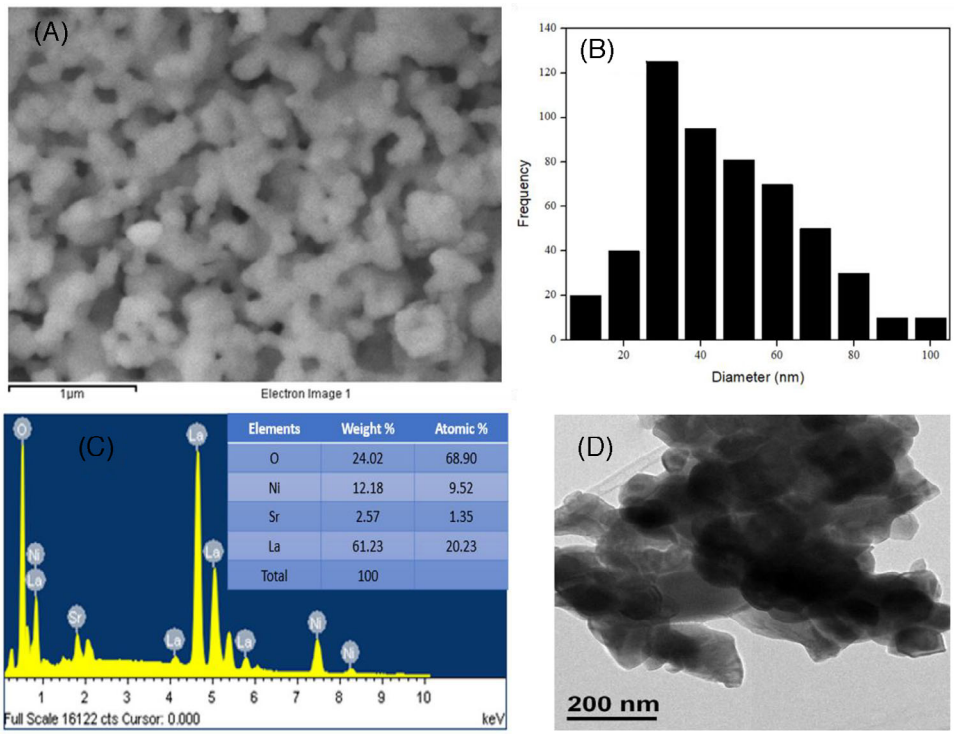

FIGURE 3 (A) Scanning electron microscopy image, (B) size distribution histogram of grains, (C) EDX micrograph with elemental analysis, and (D) high-resolution transmission electron microscopic image of LSNO perovskite. EDX, energy dispersive X-ray spectroscopy.

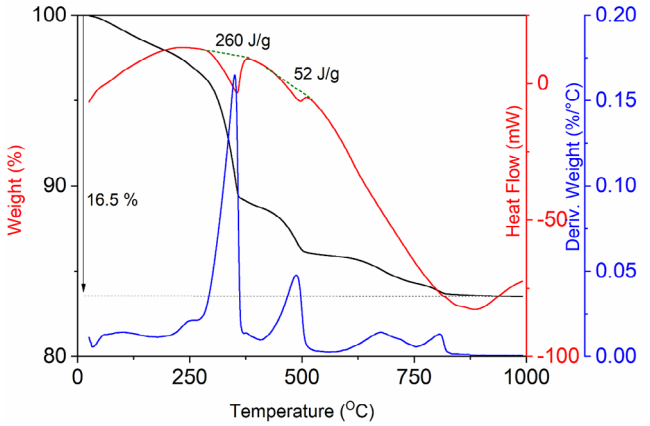

FIGURE 4 TGA–DSC graph of LSNO perovskite. DSC, differential scanning calorimetry; TGA, thermo-gravimetric.

homogenous distribution and some pores. Some agglomeration of grain can be seen, which may be due to the overlapping of small grain. The grain size distribution histogram shown in Figure 3B indicates that the average grain size is approximately 49 nm. The EDX analysis confirms the elements present at the top in LSNO, as shown in Figure 3C. The presence of all elements in LSNO confirms the purity of the synthesized material, similar to that observed in reported literature.[28]

The TEM image shown in Figure 3D indicates that the particles show aggregated faceted morphologies. The particles have a diameter size ranging between 1 and 3 μm, as measured from the TEM images. It is observed from the TEM images that the particles are connected in such a manner that forms a highly porous structure, which is responsible for the enhancement of its specific surface area, electrode contact area, and overall electrochemical performance of LSNO.[17]

The thermal stability of LSNO is important for its applications. Therefore, we performed thermo-gravimetric and differential scanning calorimetry (TGA–DSC) analyses on the sample. Figure 4 shows the weight loss occurring in four steps. The first step, a weight loss of 10.6%, occurs between 30°C–360°C and is mostly due to the absorbed water and exothermic mass loss on the DSC curve at around 360°C. The second weight loss of 3.2% taking place at around 360°C–497°C is related to the burning of excess number of organic species present in the precursor powders. A weight loss of 2.7% occurs in the range of 497°C–1000°C and sintering occurs at 814°C due to decomposition of the intermediate. These results suggest that LSNO is relatively stable around 800°C and after that, obvious decomposition occurs leading to loss of functionality.[29]

The chemical environment and compositions of the LSNO ceramic were evaluated through XPS spectra. All the detected peaks of the expected elements (and absence of any other elements) in LSNO ceramic with different respective chemical environments are represented by wide spectra in the XPS spectrum with binding energy range from 0 to 1400 eV, and is shown in Figure 5A. The presence of these elements in the LSNO ceramic was justified with the help of EDX and XRD results. Figure 5B reveals doublet peaks of La 3d spectrum namely La $3d_{5/2}$ and La $3d_{3/2}$ located at 838.2 and 851.5 eV, respectively, confirmed the existence of +3 oxidation state of La. The deconvoluted Ni 2p spectra obtained by the Gaussian fitting method for LSNO ceramic depicted in Figure 5C represents the presence of two peaks, in which one of the main peaks corresponding to Ni $2p_{3/2}$ is located at binding energy of 847.2–859.5 eV and the other peak located at 872.8 eV described Ni $3d_{1/2}$. A satellite peak is also found which corresponds with the binding energy of 860.2–869.5 eV. The peaks corresponding to the binding energy of 851.1 and 872.8 eV show the presence of Ni^{2+} state, and with the binding energy 855.2 eV, represent the +3 oxidation state of Ni (Ni^{3+}) in the LSNO ceramic.[30] The deconvoluted Sr 3d spectra were fitted with the help of the Gaussian method that depicts doublet line of Sr $3d_{5/2}$ and Sr $3d_{3/2}$, respectively in the high-resolution XPS spectrum of LSNO ceramic, are represented in Figure 5D. Both of these lines are located at 133.5 and 136.3 eV, respectively, and no other peaks were observed despite these two peaks in the Sr 3d spectra of the LSNO sample. The position of the main peak corresponding to Sr $3d_{5/2}$ located at 133.5 eV confirmed the oxidized state of Sr, reported in the earlier paper.[31] The core level high-resolution XPS spectra of O 1s elucidates three typical peaks named as O1, O2, and O3, respectively specified in Figure 5E. The respective peaks of O1, O2, and O3 are ascribed to their respective binding energy 528.7, 531.5, and 533.4 eV, which are attributed to metal–oxygen (M°C–O) bond, oxygen defect with low-O_2 coordination, and last were regarded as physisorption/chemisorbed water at the surface of the materials.[32]

3.2 | Electrocatalytic oxygen reduction reaction studies

Cyclic voltammetry (CV) and linear sweep voltammetry (LSV) responses were measured by purging with nitrogen (for nitrogen-saturated conditions) and oxygen (for oxygen-saturated conditions) for 15 min in a 100 mL electrochemical cell containing 0.1 M KOH. Figure 6 shows the CV responses for the electrocatalytic ORR at bare GCE and GCE/LSNO in the absence (i.e., nitrogen atmosphere) and presence of oxygen, with a scan rate of 20 mV/s in a potential window from 0.0 to 1.2 V (vs. RHE). The CV responses indicate that both bare GCE and GCE/LSNO exhibit no

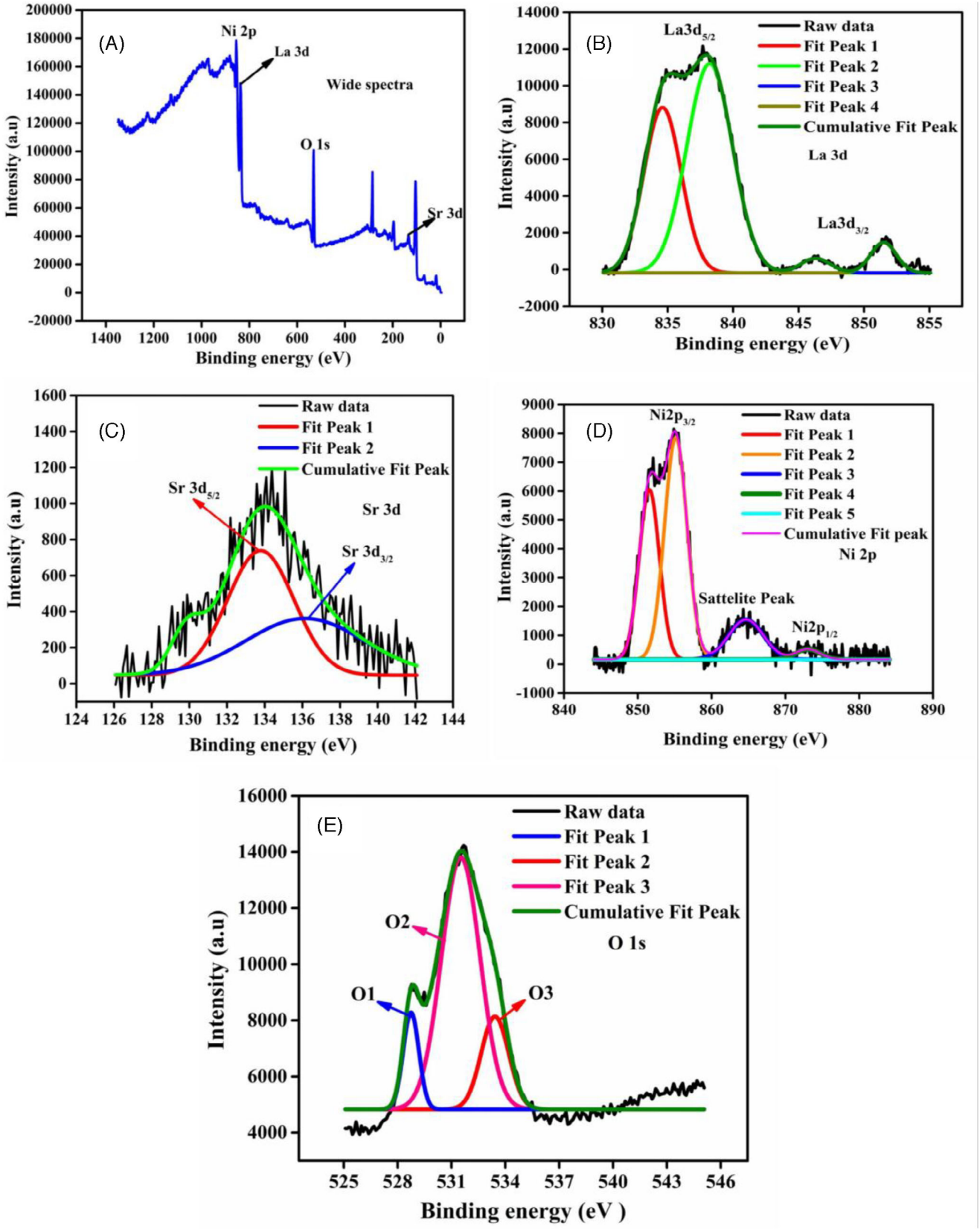

FIGURE 5 XPS, binding energy, and elemental characteristics curves (A,B,C,D and E) of LSNO perovskite. XPS, X-ray photoelectron spectroscopy.

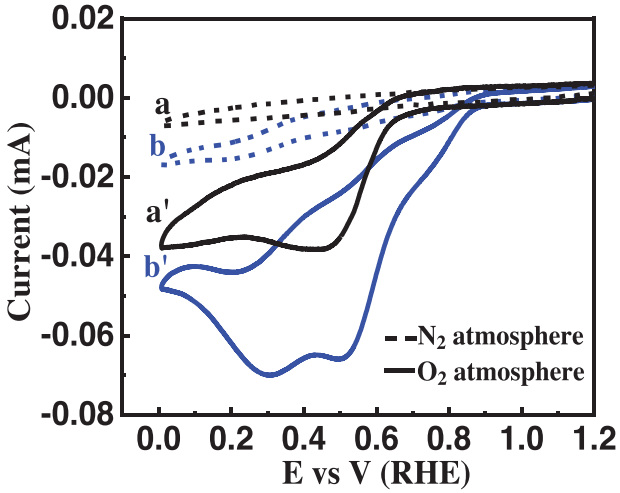

FIGURE 6 CV responses of bare GCE (a, a') and GCE/LSNO (b, b') at 20 mVs^{-1} in N_2 (a, b) and O_2 (a', b') saturated atmosphere. CV, Cyclic voltammetry; GCE, glassy carbon electrode.

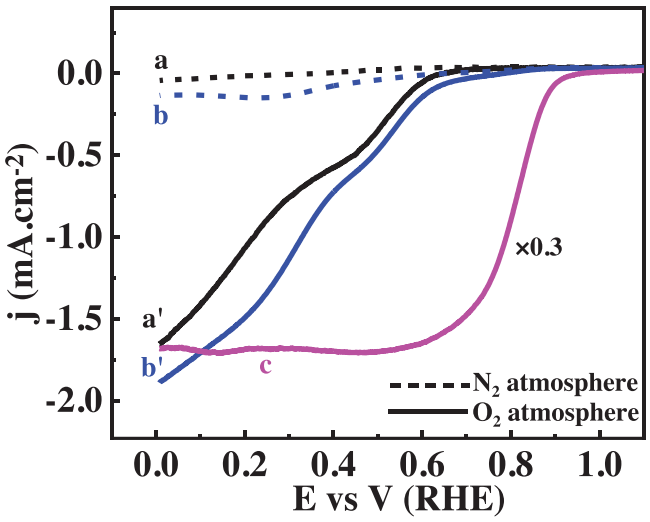

FIGURE 7 LSV polarization curves of bare GCE (a, a') and GCE/LSNO (b, b') at a scan rate of 5 mV s^{-1} and a rotation rate of 1600 rpm in N_2 (a, b) and O_2 (a', b') saturated conditions and (C) GCE/Pt-C in O_2 saturated conditions. GCE, glassy carbon electrode; LSV, linear sweep voltammetry.

significant peaks in the absence of oxygen, but a distinct peak for ORR is observed in the presence of oxygen, suggesting that GCE/LSNO has ORR activity.

The LSV responses were recorded at a scan rate of 5 mV/s and a rotation rate of 1600 rpm in the same potential window in the absence and the presence of oxygen (Figure 7). The onset potential for bare GCE (curve a and a' in Figure 7) is around 0.73 V veersus RHE, while that of GCE/LSNO (curve b and b' in Figure 7) is around 0.88 V versus RHE which are lower than Pt/C (curve c in Figure 7). Additionally, CV and LSV analysis for

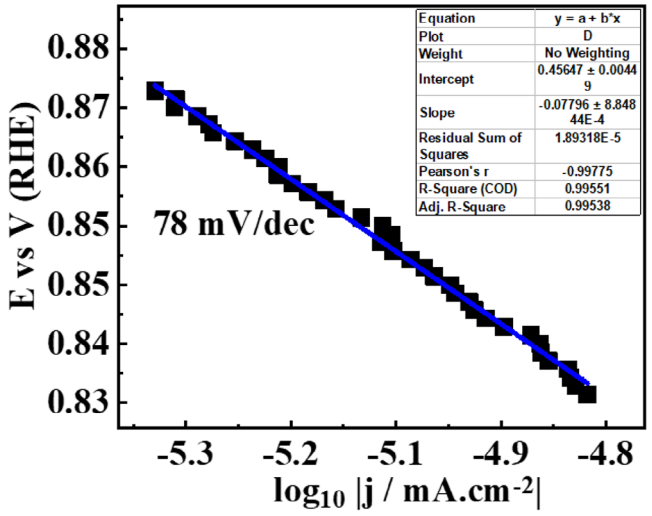

FIGURE 8 Tafel's plot for GCE/LSNO. GCE, glassy carbon electrode.

GCE/LSNO indicate that oxygen is reduced in a two-step process, in which hydrogen peroxide (H_2O_2) is formed in the first step and then reduced to water (H_2O) in the second step.[14,16] The LSV curves of GCE/LSNO also show that no plateau or limiting region is obtained, and the current density continues to increase in the negative potential region. This phenomenon is well discussed by Masa et al.[27] and Jiang et al.,[33] who indicated that it could be due to heterogeneous distribution of electrochemically active sites on the electrode surface. Since perovskites have a cage-like structure, the active sites are well embedded within the framework, resulting in a non-plateau current.

The Tafel slope values for GCE/LSNO (Figure 8) were obtained from the LSV polarization curve at 1600 rpm and were found to be 78 mV/dec. The Tafel slope obtained for GCE/LSNO is better than or comparable with many reported electrocatalysts like iron-nitrogen doped mesoporous carbon material (Fe-N-C 800 and Fe-N-C 900) showed the Tafel slope value of 100 and 108 mV/dec,[34] respectively while perovskite $LaNiO_{3-\delta}$ prepared at 800°C showed Tafel's value of 95 mV/dec.[35] Furthermore, some advanced materials like Au−Rh bimetallic nanostructures showed Tafel slope value of 57 mV/dec[36] and (cobalt tetra methoxy phenyl porphyrin (CoTMPP) immobilized on mesoporous carbon nitride showed the Tafel value of 112 mV/dec.[37]

To study the kinetics of the ORR on the GCE/LSNO electrode, a K–L plot was obtained by recording LSV polarization responses at different rotation rates (Figure 9A). The parallel nature of the K–L plots (Figure 9B) suggests that first-order kinetics are being followed for the ORR at the GCE/LSNO electrode surface.[15,38] However, the number of electrons for the ORR cannot be calculated from the K–L plot as no limiting current is observed.[39,40] The ORR

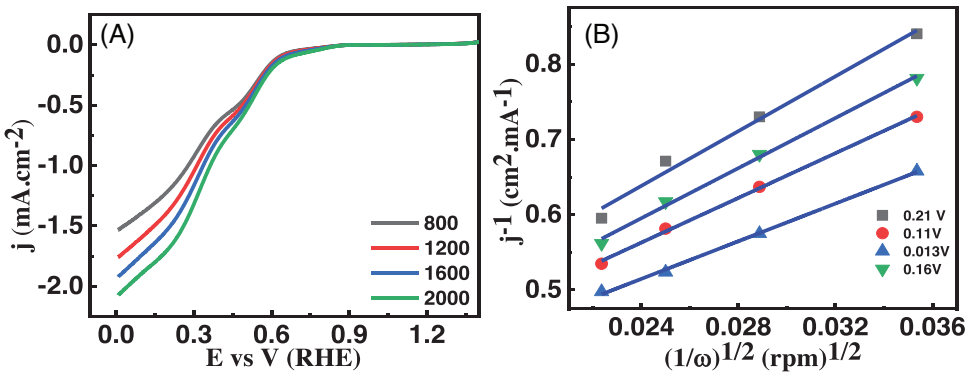

FIGURE 9 (A) LSV polarization curves of GCE/LSNO at a scan rate of 5 mV s^{-1} and at various rotation rates (800–2000 rpm) in O_2 saturated atmosphere and (B) the corresponding K–L plot. GCE, glassy carbon electrode; LSV, linear sweep voltammetry.

TABLE 2 Comparison of ORR onset potentials of various perovskites catalysts with the LSN in 0.1 M KOH.

S. No.	Catalysts	Onset potential (V vs. RHE)	References
1	$La_{0.8}Sr_{0.2}MnO_{0.3}$	0.77	27]
2	$La_{0.9}Sr_{0.1}CoO_3$	0.81	28
3	$BaTiO_{3-x}$	0.88	29
4	$BaMnO_3$	0.78 V	30
5	$(La_{0.8}Sr_{0.2})_{0.9}Mn_{0.9}Co_{0.1}O_{0.3}$	0.79 V	31
6	LSNO ($La_{1.85}Sr_{0.15}NiO_4$)	0.88 V	This work
7	$(La_{0.8}Sr_{0.2})_{0.95}Mn_{0.95}Ir_{0.05}O_3$	0.92 V	32
8	$Ba_{0.5}Sr_{0.5}Co_{0.8}Fe_{0.2}O_3$	0.78 V	33
9	$LaCo_{0.8}Mn_{0.2}O_3$	0.76 V	34
10	$La_{1.5}Sr_{0.5}NiMn_{0.5}Ru_{0.5}O_6$	0.94 V	35

Abbreviation: ORR, oxygen reduction reaction.

activity of LSNO is compared with other perovskite-based electrocatalysts (Table 2) under similar conditions and the onset potential (0.88 V vs. RHE) of LSNO is found to be better than many reported perovskite-based catalysts, such as $La_{0.8}Sr_{0.2}MnO_3$,[41] $La_{0.9}Sr_{0.1}CoO_3$,[42] $BaMnO_3$,[43] $(La_{0.8}Sr_{0.2})_{0.9}Mn_{0.9}Co_{0.1}O_{0.3}$,[44] $Ba_{0.5}Sr_{0.5}Co_{0.8}Fe_{0.2}O_3$,[45] and $LaCo_{0.8}Mn_{0.2}O_3$.[46] LSNO electrocatalyst shows onset potential comparable to $BaTiO_{3-x}$.[47] However, perovskites $(La_{0.8}Sr_{0.2})_{0.95}Mn_{0.95}Ir_{0.05}O_3$[44] and $La_{1.5}Sr_{0.5}NiMn_{0.5}Ru_{0.5}O_6$[48] which consist of expensive metals (Ir or Ru), show slightly higher onset potentials than the LSNO electrocatalyst.

3.3 | Supercapacitor

Perovskite oxides possess unique energy storage capabilities. In this work, we attempted to prepare LSNO through a simple one-pot method, which could significantly reduce the cost of material preparation. It has been observed in previous studies that defects can arise during the synthesis process due to thermal fluctuations, which disrupt the periodicity of perovskites and result in lattice positions becoming vacant. These defects introduce useful properties for energy storage applications such as batteries, SCs, SOFCs, and solar cells. The electrochemical properties of $La_{1.85}Sr_{0.15}NiO_4$ perovskite as an electrode material were analyzed using CV and galvanostatic charge–discharge (GCD). Figure 10A plots the current density against potential for scan rates ranging from 2 to 50 mV/s in a 1 M Na_2SO_4 electrolyte. The CV curves are quasi-rectangular, which suggests effective reversible capacitive behavior, but they do not resemble the ideal shape for an electric double-layer capacitance (EDLC).

So, it can be stated that the capacitance is of EDLC type with probability of some contribution of pseudo capacitance. The mechanism of charge storage is due to the contribution of both EDLC and Faradaic reactions (pseudo capacitance) on the overall capacitance. The CV curve demonstrates general characteristics with a fast charge–discharge rate. The increase in scan rate increases the current density, indicating that the redox processes are primarily governed by ion insertion and de-insertion. The CV graphs are nearly symmetrical, which makes the samples

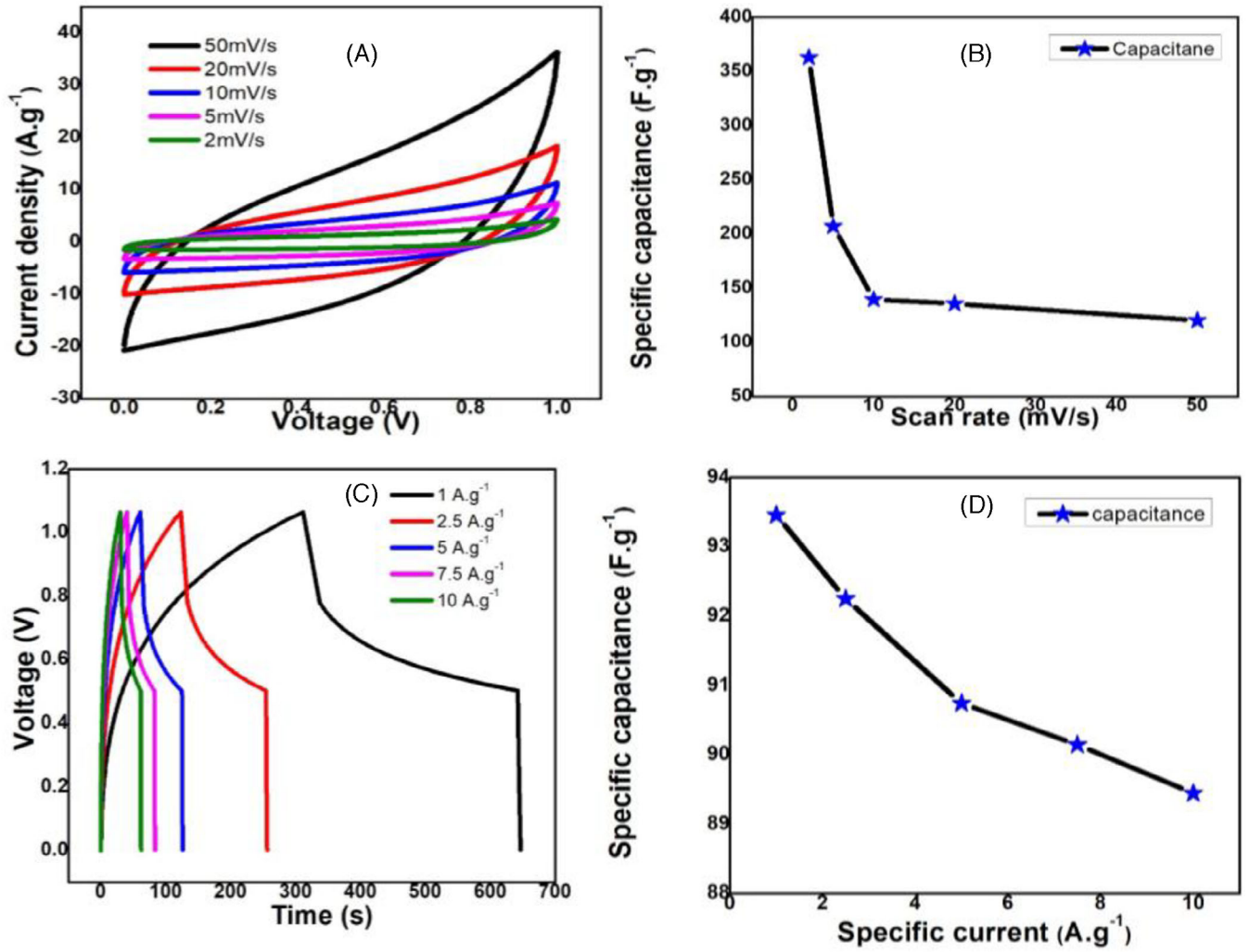

FIGURE 10 (A) CV curves with 1 M Na_2SO_4 electrolyte at different scan rates ranging from 2 to 50 mV/s and (B) variation of specific capacitance (obtained from CV curves) with scan rate of LSNO electrode. (C) GCD curves with different specific current density and (D) variation of specific capacitance (obtained from GCD curves) with specific current of LSNO electrode. CV, Cyclic voltammetry; GCD, galvanostatic charge–discharge.

highly suitable as electrodes for excellent SCs. The specific capacitance of our samples was calculated from the graph using Equation (5)[49]:

$$C_{SC} = \frac{1}{m\upsilon(V_b - V_a)} \int_{V_a}^{V_b} I(V)dV \quad (5)$$

where C_{SC} denotes the specific capacitance, m for the mass of the $La_{1.85}Sr_{0.15}NiO_4$ at the electrode surface, υ for the scan rate, $(V_b - V_a)$ for the potential window, and I for the current response of electrode in electrolyte.

Table 3 displays the specific capacitance values determined from the CV curves for various scan rates. The specific capacitance values are satisfactory and comparable. The value of specific capacitance of perovskites is primarily due to the contribution of EDLC, which arises from the charge–discharge process at the surface of the electrolyte–electrode material.[50–52]

TABLE 3 Scan rate vs. specific capacitance.

Scan rate (mV/s)	Specific capacitance (F g^{-1})
2	362.86
5	207.07
10	139.55
25	135.70
50	120.20

As seen in Figure 10B, the specific capacitance of the electrode material decreases with increasing scan rates. This is because at low scan rates, ions have adequate time to diffuse into the surface of the electrode material, allowing both the outer and inner pore-surfaces to be

TABLE 4 Specific capacitance from GCD curves.

Specific current (A g^{-1})	Specific capacitance (F g^{-1})
1.0	93.46
2.5	92.25
5.0	90.74
7.5	90.14
10.0	89.45

Abbreviation: GCD, galvanostatic charge–discharge.

utilized effectively. However, at high scan rates, ions have limited time to intercalate into the surface of the electrode, and only the outer pore-surface is utilized, resulting in a decrease in the specific capacitance of the electrode material. This is referred to as the ion-exchange mechanism.[53]

The GCD method is performed under the same electrode–electrolyte conditions as the CV for the electrode sample. Figure 10C shows the charge/discharge curve of the $La_{1.85}Sr_{0.15}NiO_4$ perovskite as an electrode material at different current densities. The nonlinearity of the charge and discharge curves reveals the EDLC behavior of the electrode material. In the GCD curves, we can see that the discharge part has two different slopes: one for rapid discharge caused by IR drop and the other for a slow decay. The specific capacitance value of the electrode can be calculated from the GCD curve using Equation (2).

$$C_s = \frac{4I\Delta t}{m\Delta V}, \tag{6}$$

where m denotes for mass of the electrode material, I for the current density, Δt for discharge time, and ΔV for potential window.

The specific capacitance calculated from the GCD graph is reported in Table 4. The decrease in specific capacitance with increasing current density (Figure 10D) is due to the effect of ohmic drop and slow kinetics of the charge–discharge and separation of ion mechanism.[54] The rise in charge mobility with increasing current density also contributes to this decrease. As the sample was prepared in a novel manner, future variations in the elements are possible for optimization of the electrochemical performance.

Cyclic stability is critical for the practical implementation of energy storage devices, so we synthesized the material in a way that they can be used as an efficient electrode with good cyclic stability. The capacity retention curve (Figure S1) demonstrates that the specific capacity remains nearly constant throughout all ranges of cyclic numbers. After 500 cycles, the LSNO electrode retained 97.25% of its specific capacitance, which can be ascribed to the reduced agglomeration of nanoparticles for larger cyclic numbers.

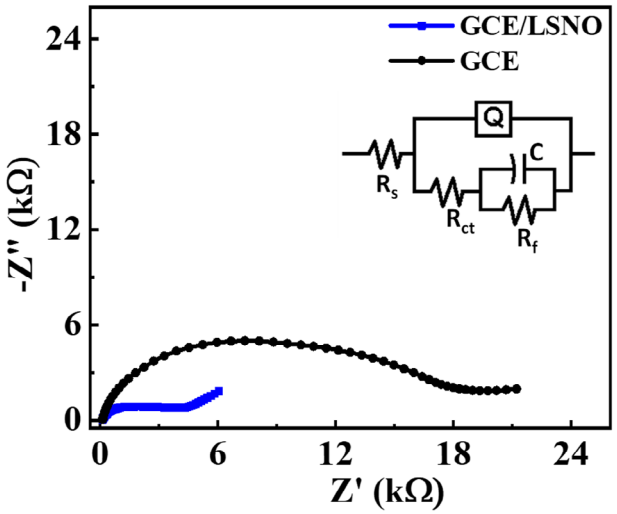

FIGURE 11 EIS responses of GCE and GCE/LSNO fitted in $R(Q(R(CR)))$ equivalent circuit, where the R_s denotes the solution resistance, Q denotes a constant phase element, R_{ct} signifies charge transfer resistance, C indicates capacitance, and the R_f indicates film resistance. GCE, glassy carbon electrode; EIS, electrochemical impedance spectroscopy.

Electrochemical impedance spectroscopy (EIS) responses were recorded in a solution of 10 mM $Fe^{2+/3+}$ with 0.1 M KCl. The EIS data were best fitted using an equivalent circuit represented as $R(Q(R(CR)))$, where the first R denotes the solution resistance (R_s), Q represents a constant phase element, the second R signifies charge transfer resistance (R_{ct}), C denotes capacitance, and the third R indicates film resistance (R_f). Figure 11 illustrates the Nyquist plot of GCE and GCE/LSNO. The charge transfer resistance (R_{ct}) for GCE/LSNO was measured as 100 Ω, whereas for the bare GCE it was found to be 174.3 Ω. This indicates that the LSNO material exhibits superior conductivity compared to the unmodified GCE.

Furthermore, BET surface analysis was carried out to measure the surface area and porosity of electrode materials. Surface area has a significant impact on the properties of nanomaterials[55] and the defects in the samples often make them efficient electrode materials for energy storage. The effective surface area and pore size of the LSNO sample were analyzed by nitrogen gas adsorption/desorption at −196°C using the BET measurement technique. The total active specific surface area was about 20.14 m^2 g^{-1}. The variation of pore volume with pore size is shown in Figure S2.

4 | CONCLUSIONS

In this study, we investigated the synthesis of $La_{1.85}Sr_{0.15}NiO_4$ (LSNO) perovskite material using an

economical and novel one-step approach under ambient conditions, without the need for a multi-step process or external energy source. The LSNO produced had high purity and crystallinity, and was sintered at a temperature of 900°C for 12 h. XRD results confirmed the formation of a crystalline perovskite phase, while infrared spectrum showed no evidence of secondary phases. High-resolution transmission electron microscopy revealed a homogeneous size distribution of nanometric LSNO powders. The highly crystalline and thermally stable tetragonal structure of LSNO provides enhanced oxygen reduction and evolution reactions, as well as improved SC performance. The bi-functional properties of LSNO as an electrocatalytic material and electrochemical SC open up new avenues for designing and synthesizing multifunctional perovskites-based materials.

ACKNOWLEDGMENTS

Dr. Laxman Singh is grateful to Siddharth University for the minor project (ID: SMGFOC/2023-24/FS-005) and the Council of Science and Technology, Lucknow, Uttar Pradesh for the funding of the project (ID: 4287). This study was supported by the Basic Science Research Program through the National Research Foundation of Korea (NRF) funded by the MSIT (2021R1A2C1010373) and the MOE (2021R1A6A1A03038858).

CONFLICT OF INTEREST STATEMENT

The authors declare no conflicts of interest.

DATA AVAILABILITY STATEMENT

Data will be made available on request.

ORCID

Laxman Singh https://orcid.org/0000-0003-3297-6625

REFERENCES

1. Kumar S, Rai RN, Singh D, Ansari AA, Lee Y, Singh L. Future perspectives on QDs embedded nano-fibrous materials as high capacity sustainable anode for Na-ion batteries technology. MRS Energy Sustain. 2023;10:238–46. https://doi.org/10.1557/s43581-023-00067-x
2. Sridhar S, Salkuti SR. Development and future scope of renewable energy and energy storage systems. Smart Cities. 2022;5:668–99. https://doi.org/10.3390/smartcities5020035
3. Singh L, Dhavala L, Bhimireddi R, Ansari AA, Kumar S, Srivastava V, et al. Low-cost flame synthesized $La_{2/3}Cu_3Ti_4O_{12}$ electro-ceramic and extensive investigation on electrical, impedance, modulus, and optical properties. Ceram Int. 2023;49:21795–803. https://doi.org/10.1016/j.ceramint.2023.04.001
4. Saraswat A, Kumar S. Cutting-edge applications of polyaniline composites towards futuristic energy supply devices. Eur Polym J. 2023;200:112501. https://doi.org/10.1016/j.eurpolymj.2023.112501
5. Rao P, Wu D, Wang TJ, Li J, Deng P, Chen Q, et al. Single atomic cobalt electrocatalyst for efficient oxygen reduction reaction. EScience. 2022;2:399–404. https://doi.org/10.1016/j.esci.2022.05.004
6. Han M, Gómez-Recio I, Martín DG, Ortiz Peña N, Ruiz-González ML, Selmane M, et al. Tuning of oxygen electrocatalysis in perovskite oxide nanoparticles by the cationic composition. ACS Catal. 2023;13:5733–43. https://doi.org/10.1021/acscatal.3c00461
7. Thomas SA, Patra A, Al-Shehri BM, Selvaraj M, Aravind A, Rout CS. MXene based hybrid materials for supercapacitors: recent developments and future perspectives. J Energy Storage. 2022;55:105765. https://doi.org/10.1016/j.est.2022.105765
8. Subhani K, Hameed N, Al-Qatatsheh A, Ince J, Mahon PJ, Lau A, et al. Multifunctional structural composite supercapacitors based on MnO_2-nanowhiskers decorated carbon fibers. J Energy Storage. 2022;56:105936. https://doi.org/10.1016/j.est.2022.105936
9. Kumar S, Maiti P. Review on functional electrolyte, redox polymers, and solar conversions in 3G emerging photovoltaic technologies: progress and outlook. Energy Fuels. 2023;37:14473–511. https://doi.org/10.1021/acs.energyfuels.3c01695
10. Li Z, Li M, Zhu Z. Perovskite cathode materials for low-temperature solid oxide fuel cells: fundamentals to optimization. Electrochem Energy Rev. 2022;5:263–311. https://doi.org/10.1007/s41918-021-00098-3
11. Saraswat A, Kumar S. A topical study of electrochemical response of functionalized conducting polyaniline: an overview. Eur Polym J. 2023;182:111714. https://doi.org/10.1016/j.eurpolymj.2022.111714
12. Xu Z, Deng W, Wang X. 3D Hierarchical carbon-rich micro-/nanomaterials for energy storage and catalysis. Electrochem Energy Rev. 2021;4:269–335. https://doi.org/10.1007/s41918-021-00094-7
13. Zhou J, Xia Z, Molokeev MS, Zhang X, Peng D, Liu Q. Composition design, optical gap and stability investigations of lead-free halide double perovskite $Cs_2AgInCl_6$. J Mater Chem A. 2017;5:15031–37. https://doi.org/10.1039/c7ta04690a
14. Kim HW, Bukas VJ, Park H, Park S, Diederichsen KM, Lim J, et al. Mechanisms of two-electron and four-electron electrochemical oxygen reduction reactions at nitrogen-doped reduced graphene oxide. ACS Catal. 2020;10:852–63. https://doi.org/10.1021/acscatal.9b04106
15. Yadav M, Sonkar PK, Prakash K, Ganesan V, Sankar M, Yadav DK, et al. Insight into efficient bifunctional catalysis: oxygen reduction and oxygen evolution reactions using MWCNTs based composites with 5,10,15,20-tetrakis(3′,5′-dimethoxyphenyl)porphyrinato cobalt(II) and 5,10,15,20-tetrakis(3′,5′-dihydroxyphenyl)porphyrinato cobalt(II). Int J Hydrogen Energy. 2020;45:9710–22. https://doi.org/10.1016/j.ijhydene.2020.01.224
16. Ashok A, Kumar A, Bhosale RR, Almomani F, Malik SS, Suslov S, et al. Combustion synthesis of bifunctional $LaMO_3$ (M = Cr, Mn, Fe, Co, Ni) perovskites for oxygen reduction and oxygen evolution reaction in alkaline media. J Electroanal Chem. 2018;809:22–30. https://doi.org/10.1016/j.jelechem.2017.12.043
17. Jinlong L, Miura H, Meng Y. A novel mesoporous $NiMoO_4$@rGO nanostructure for supercapacitor applications.

Mater Lett. 2017;194:94–97. https://doi.org/10.1016/j.matlet.2017.02.040
18. Chen Y, Nie X, Wang B, Xia C, Dong W, Wang X, et al. Tuning $La_{0.6}Sr_{0.4}Co_{0.2}Fe_{0.8}O_{3-\delta}$ perovskite cathode as functional electrolytes for advanced low-temperature SOFCs. Catal Today. 2020;355:295–303. https://doi.org/10.1016/j.cattod.2019.05.064
19. Cao Y, Lin B, Sun Y, Yang H, Zhang X. Sr-doped lanthanum nickelate nanofibers for high energy density supercapacitors. Electrochim Acta. 2015;174:41–50.
20. Qayyum A, ur Rehman MO, Ahmad F, Khan MA, Ramay SM, Atiq S. Performance optimization of Nd-doped $LaNiO_3$ as electrode material in supercapacitors. Solid State Ionics. 2023;395:116227.
21. Cao Y, Lin B, Sun Y, Yang H, Zhang X. Symmetric/asymmetric supercapacitor based on the perovskite-type lanthanum cobaltate nanofibers with Sr-substitution. Electrochim Acta. 2015;178:398–406.
22. Maruta J, Yasuda H, Yamachi M. Low-temperature synthesis of lithium nickelate positive active material from nickel hydroxide for lithium cells. J Power Sources. 2000;90:89–94. https://doi.org/10.1016/S0378-7753(00)00453-5
23. Forslund RP, Pender J, Alexander CT, Johnston KP, Stevenson KJ. Comparison of perovskite and perovskite derivatives for use in anion-based pseudocapacitor applications. J Mater Chem A. 2019;7:21222–31.
24. Gopi UV, Reddi US, Karthik M, Smaran KS. Controlling phase transformation of La/Ni oxides by switching annealing conditions and their resultant pseudocapacitive behaviour. Nanotechnology. 2023;35(8):085402.
25. Rodriguez-Carvajal J, Fernandez-Diaz MT, Martinez JL. Neutron diffraction study on structural and magnetic properties of La_2NiO_4. J Phys: Condens Matter. 1991;3:3215–34
26. Kumar V, Kumari S, Kumar P, Kar M, Kumar L. Structural analysis by Rietveld method and its correlation with optical properties of nanocrystalline zinc oxide. Adv Mater Lett. 2015;6(2):139–47.
27. Masa J, Schilling T, Bron M, Schuhmann W. Electrochemical synthesis of metal-polypyrrole composites and their activation for electrocatalytic reduction of oxygen by thermal treatment. Electrochim Acta. 2012;60:410–18. https://doi.org/10.1016/j.electacta.2011.11.076
28. Wang H, Zhou M, Choudhury P, Luo H. Perovskite oxides as bifunctional oxygen electrocatalysts for oxygen evolution/reduction reactions—a mini review. Appl Mater Today. 2019;16:56–71. https://doi.org/10.1016/j.apmt.2019.05.004
29. Singh L, Sin BC, Kim IW, Mandal KD, Chung H, Lee Y. A novel one-step flame synthesis method for tungsten-doped CCTO. J Am Ceram Soc. 2016;99:27–34. https://doi.org/10.1111/jace.13930
30. Cheng M, Fan H, Song Y, Cui Y, Wang R. Interconnected hierarchical $NiCo_2O_4$ microspheres as high-performance electrode materials for supercapacitors. Dalt Trans. 2017;46:9201–9. https://doi.org/10.1039/c7dt01289f
31. Suchaneck G, Kalanda N, Artiukh E, Yarmolich M, Sobolev NA. Tunneling conduction mechanisms in strontium ferromolybdate ceramics with strontium molybdate dielectric intergrain barriers. J Alloys Compd. 2021;860:158526. https://doi.org/10.1016/j.jallcom.2020.158526
32. An C, Wang Y, Huang Y, Xu Y, Jiao L, Yuan H. Porous $NiCo_2O_4$ nanostructures for high performance supercapacitors via a microemulsion technique. Nano Energy. 2014;10:125–34. https://doi.org/10.1016/j.nanoen.2014.09.015
33. Jiang R, Anson FC. The origin of inclined plateau currents in steady-state voltammograms for electrode processes involving electrocatalysis. J Electroanal Chem. 1991;305:171–84. https://doi.org/10.1016/0022-0728(91)85516-R
34. Li C, He C, Sun F, Wang M, Wang J, Lin Y. Incorporation of Fe_3C and pyridinic N active sites with a moderate N/C ratio in Fe–N mesoporous carbon materials for enhanced oxygen reduction reaction activity. ACS Appl Nano Mater. 2018;1:1801–10. https://doi.org/10.1021/acsanm.8b00235
35. Zhou W, Sunarso J. Enhancing bi-functional electrocatalytic activity of perovskite by temperature shock: a case study of $LaNiO_{3-\delta}$. J Phys Chem Lett. 2013;4:2982–88. https://doi.org/10.1021/jz401169n
36. Narayanamoorthy B, Balaji S, Sita C, Pasupathi S, Eswaramoorthy M, Moon IS. Enhanced intrinsic activity and stability of Au–Rh bimetallic nanostructures as a supportless cathode electrocatalyst for oxygen reduction in alkaline fuel cells. ACS Sustain Chem Eng. 2016;4:6480–90. https://doi.org/10.1021/acssuschemeng.6b01257
37. Singh DK, Ganesan V, Yadav DK, Yadav M, Sonkar PK, Gupta R. Mesoporous carbon nitride supported 5,10,15,20-tetrakis(4-methoxyphenyl)-21H,23H-porphine cobalt(ii) as a selective and durable electrocatalyst for the production of hydrogen peroxideviatwo-electron oxygen reduction. Catal Sci Technol. 2021;11:1014–26. https://doi.org/10.1039/d0cy01801e
38. Lin Y, Cui X, Ye X. Electrocatalytic reactivity for oxygen reduction of palladium-modified carbon nanotubes synthesized in supercritical fluid. Electrochem Commun. 2005;7:267–74. https://doi.org/10.1016/j.elecom.2005.01.007
39. Singh DK, Ganesan V, Yadav DK, Yadav M. Metal (Mn, Fe, Co, Ni, Cu, and Zn) phthalocyanine-immobilized mesoporous carbon nitride materials as durable electrode modifiers for the oxygen reduction reaction. Langmuir. 2020;36:12202–12. https://doi.org/10.1021/acs.langmuir.0c01822
40. Zhou R, Zheng Y, Jaroniec M, Qiao SZ. Determination of the electron transfer number for the oxygen reduction reaction: from theory to experiment. ACS Catal. 2016;6:4720–28. https://doi.org/10.1021/acscatal.6b01581
41. Jin C, Cao X, Zhang L, Zhang C, Yang R. Preparation and electrochemical properties of urchin-like $La_{0.8}Sr_{0.2}MnO_3$ perovskite oxide as a bifunctional catalyst for oxygen reduction and oxygen evolution reaction. J Power Sources. 2013;241:225–30. https://doi.org/10.1016/j.jpowsour.2013.04.116
42. Bie S, Zhu Y, Su J, Jin C, Liu S, Yang R, et al. One-pot fabrication of yolk–shell structured $La_{0.9}Sr_{0.1}CoO_3$ perovskite microspheres with enhanced catalytic activities for oxygen reduction and evolution reactions. J Mater Chem A. 2015;3:22448–53. https://doi.org/10.1039/c5ta05271h
43. Xu Y, Tsou A, Fu Y, Wang J, Tian JH, Yang R. Carbon-coated perovskite $BaMnO_3$ porous nanorods with enhanced electrocatalytic perporites for oxygen reduction and oxygen evolution. Electrochim Acta. 2015;174:551–56. https://doi.org/10.1016/j.electacta.2015.05.184
44. Xu W, Yan L, Teich L, Liaw S, Zhou M, Luo H. Polymer-assisted chemical solution synthesis of $La_{0.8}Sr_{0.2}MnO_3$-based perovskite with A-site deficiency and cobalt-doping for bifunctional oxygen

catalyst in alkaline media. Electrochim Acta. 2018;273:80–87. https://doi.org/10.1016/j.electacta.2018.04.046

45. Jin C, Cao X, Lu F, Yang Z, Yang R. Electrochemical study of $Ba_{0.5}Sr_{0.5}Co_{0.8}Fe_{0.2}O_3$ perovskite as bifunctional catalyst in alkaline media. Int J Hydrogen Energy. 2013;38:10389–93. https://doi.org/10.1016/j.ijhydene.2013.06.047
46. Ge X, Li B, Wuu D, Sumboja A, An T, Hor TSA, et al. Nanostructured perovskite $LaCo_{1-x}Mn_xO_3$ as bifunctional catalysts for rechargeable metal–air batteries. J Mol Eng Mater. 2015;03:1540006. https://doi.org/10.1142/s2251237315400067
47. Chen CF, King G, Dickerson RM, Papin PA, Gupta S, Kellogg WR, et al. Oxygen-deficient $BaTiO_{3-x}$ perovskite as an efficient bifunctional oxygen electrocatalyst. Nano Energy. 2015;13:423–32. https://doi.org/10.1016/j.nanoen.2015.03.005
48. Retuerto M, Calle-Vallejo F, Pascual L, Lumbeeck G, Fernandez-Diaz MT, Croft M, et al. $La_{1.5}Sr_{0.5}NiMn_{0.5}Ru_{0.5}O_6$ double perovskite with enhanced ORR/OER bifunctional catalytic activity. ACS Appl Mater Interfaces. 2019;11:21454–64. https://doi.org/10.1021/acsami.9b02077
49. Jin G, Xiao X, Li S, Zhao K, Wu Y, Sun D, et al. Strongly coupled graphene/Mn_3O_4 composite with enhanced electrochemical performance for supercapacitor electrode. Electrochim Acta. 2015;178:689–98. https://doi.org/10.1016/j.electacta.2015.08.032
50. Liu Y, Wang Z, Veder JPM, Xu Z, Zhong Y, Zhou W, et al. Highly defective layered double perovskite oxide for efficient energy storage via reversible pseudocapacitive oxygen–anion intercalation. Adv Energy Mater. 2018;8:1702604. https://doi.org/10.1002/aenm.201702604
51. Kostopoulou A, Kymakis E, Stratakis E. Perovskite nanostructures for photovoltaic and energy storage devices. J Mater Chem A. 2018;6:9765–98. https://doi.org/10.1039/c8ta01964a
52. Mo H, Nan H, Lang X, Liu S, Qiao L, Hu X, et al. Influence of calcium doping on performance of $LaMnO_3$ supercapacitors. Ceram Int. 2018;44:9733–41. https://doi.org/10.1016/j.ceramint.2018.02.205
53. Pang H, Deng J, Wang S, Li S, Du J, Chen J, et al. Facile synthesis of porous nickel manganite materials and their morphology effect on electrochemical properties. RSC Adv. 2012;2:5930–34. https://doi.org/10.1039/c2ra20245j
54. Pendashteh A, Rahmanifar MS, Kaner RB, Mousavi MF. Facile synthesis of nanostructured $CuCo_2O_4$ as a novel electrode material for high-rate supercapacitors. Chem Commun. 2014;50:1972–75. https://doi.org/10.1039/c3cc48773c
55. Xia H, Wang Y, Lin J, Lu L. Hydrothermal synthesis of MnO_2/CNT nanocomposite with a CNT core/porous MnO_2 sheath hierarchy architecture for supercapacitors. Nanoscale Res Lett. 2012;7:33. https://doi.org/10.1186/1556-276X-7-33

SUPPORTING INFORMATION

Additional supporting information can be found online in the Supporting Information section at the end of this article.

How to cite this article: Singh L, Patel VK, Mukherjee A, Singh V, Kumar A, Rai A, et al. One-pot instant flame synthesis of strontium-doped lanthanum nickelate perovskite for energy conversion and storage. J Am Ceram Soc. 2025;108:e70046. https://doi.org/10.1111/jace.70046